Microsc. Microanal. Page 1 of 10
doi:10.1017/S1431927613001888

Microscopy AND Microanalysis

Phase Classification by Mean Shift Clustering of Multispectral Materials Images

Diego Schmaedech Martins,[1] Victor M. Galván Josa,[2,3] Gustavo Castellano,[2,3] and José A.T. Borges da Costa[4,*]

[1]*Programa de Pós-Graduação em Informática, Universidade Federal de Santa Maria, 97105-900 Santa Maria, RS, Brazil*
[2]*FaMAF, Universidad Nacional de Córdoba, Medina Allende s/n, Ciudad Universitaria, 5000 Córdoba, Argentina*
[3]*IFEG-CONICET, Medina Allende s/n, Ciudad Universitaria, 5000 Córdoba, Argentina*
[4]*Departamento de Física, Universidade Federal de Santa Maria, 97105-900 Santa Maria, RS, Brazil*

Abstract: A mean-shift clustering (MSC) algorithm is introduced as a valuable alternative to perform materials phase classification from multispectral images. As opposed to other multivariate statistical techniques, such as factor analysis or principal component analysis (PCA), clustering techniques directly assign a class label to each pixel, so that their outputs are phase segmented images, i.e., there is no need for an additional segmentation algorithm. On the other hand, as compared to other clustering procedures and classification methods, such as segmentation by thresholding of multiple spectral components, MSC has the advantages of not requiring previous knowledge of the number of data clusters and not assuming any shape for these clusters, i.e., neither the number nor the composition of the phases must be previously known. This makes MSC a particularly useful tool for exploratory research, assisting phase identification of unknown samples. Visualization and interpretation of the results are also simplified, since the information content of the output image does not depend on the particular choice of the content of the color channels. We applied MSC to the analysis of two sets of X-ray maps acquired in scanning electron microscopes equipped with energy-dispersive detection systems. Our results indicate that MSC is capable of detecting additional phases, not clearly identified through PCA or multiple thresholding, with a very low empirical reject rate.

Key words: phase classification, X-ray maps, SEM, image segmentation, mean-shift clustering

Introduction

The aim of phase classification is to determine the spatial distributions of the components or phases within heterogeneous materials samples. By its nature, this task is usually accomplished by using chemical composition maps, or images whose intensities correlate with chemical composition and/or structure, obtained with the aid of local probe techniques. Also, phase identification in unknown samples could be performed if quantitative maps or intensity calibrated images are analyzed in association with a database.

X-ray maps (XRMs), obtained by collecting characteristic X-rays from induced radiative transitions of the elements present in a sample, are particularly useful for gathering elemental distribution. Usually, the excitation source is an electron beam, which is scanned in a raster across the specimen while X-ray intensities are recorded as pixel gray levels in an 8-bit register proportional to the physical intensity value.

The spatial resolution of XRMs is limited by the interaction volume, which is around 2 μm diameter, depending on the electron beam energy, the overall sample composition, and the particular element being mapped. The acquisition time required for registering an XRM with 256×256 pixels and reasonable statistical uncertainties is about 30 min (at 20 kcps). Larger maps take longer: a more acceptable 512×512 pixel map acquisition, e.g., may last around 2 h. Recent advances in energy-dispersive spectrometry (EDS) have resulted in detector systems with higher counting rates. Silicon drift detectors, e.g., can produce high quality images at 60 kcps in a few minutes (Gernet, 2008). The XRMs acquired with EDS allow the detection of elements present in concentrations higher than 100 ppm.

Backscattered electron (BSE) images are also useful to determine the number and distribution of phases, since the gray level of each pixel is related to the mean atomic number at the corresponding position on the sample surface. QEMSCAN instruments perform phase segmentation by gray level thresholding of BSE images followed by analysis of the corresponding energy-dispersive X-ray spectra. Even though the BSE signal is proportional to the average atomic number of the sample volume examined, chemical composition is not taken into account from the beginning. Chemistry of the particles is investigated only after segmentation. This approach became popular in the last decade (Allen et al., 2012; Carling et al., 2012) and works well when there is no overlap of the BSE histograms of the phases. Information about the crystalline structure can be obtained with the aid of other techniques like electron backscatter diffraction (Humphreys, 2001) and transmission electron microscopy. Nevertheless, costs and difficulties associated with sample preparation inhibit their frequent use.

Phase contrast can also be produced by cathodoluminescence (CL), which can be conducted both in a scanning

Received March 15, 2012; accepted May 7, 2013
*Corresponding author. E-mail: juca@smail.ufsm.br

electron microscope (SEM), or in an optical microscope with specialized optical detectors. CL multispectral images contain information on the composition, structure, and trace elements. In a SEM, CL images can be acquired simultaneously with XRMs, allowing the combination of information from different analytical techniques (MacRae et al., 2005). Calibrated multispectral imaging has also been conducted in optical microscopy for the identification of ore minerals (Pirard, 2004) and iron oxides (Pirard & Lebichot, 2005).

There are several techniques for the treatment of multispectral images, as well as multimodal images produced by the above techniques. Composite color images (Russ, 2006), made by assigning different spectral components to each color channel in an RGB image, is the most commonly used visualization technique, which may also provide phase identification, depending on the sample properties and on the metainformation available.

Segmentation by thresholding of multiple spectral components has been applied to quantitative determination of mineral abundance in geological samples from CL images (Götze et al., 1997) and to the identification of cement phases from XRMs (Bentz et al., 1999). The latter problem has also been approached by Ding and Colpan (2006), who applied a decision tree induction model for partitioning the feature space of spectral components.

Multivariate statistical analysis methods have also been applied to X-ray spectral images (Kotula, 2002; Kotula et al., 2003; Kotula & Keenan, 2006). Principal component analysis (PCA) is a useful technique for extracting the maximum contrast and structural information from a set of images. It is a mathematical procedure that uses an orthogonal transformation to convert a set of observations of possibly correlated variables into a set of values of uncorrelated variables called principal components (Harris, 2001). PCA can be applied to multispectral images to produce visual representations of the phase distribution by assigning each of the most significant components to a color channel (Neal & Russ, 2004; Russ, 2006). However, it is important to be aware that principal components do not correspond to phases and their linear coefficients are not relative abundances of the elements. As shown by Keenan (2008), factor rotation can be an effective strategy for deriving physically realistic factors that are more easily interpreted than the abstract factors obtained via PCA. However, the output is not a phase segmented image, so that phase classification on a pixel-by-pixel basis requires further processing and analysis.

In a recent paper, Stork & Keenan (2010) have pointed out the advantages of clustering (Jain, 2010) in the phase classification of multispectral materials images, when applying fuzzy cluster means (FCM) to XRMs of a solder bump and a braze interface. In FCM each pixel has a degree of membership in each cluster, identified by the corresponding spectral profile, or prototype. Both the membership values and cluster prototypes are iteratively determined in order to minimize an objective function. Classification is achieved by assigning each pixel to the cluster in which it has the highest fuzzy membership value.

Mean shift is a general purpose iterative procedure for finding data clusters in multivariate datasets, originally described by Fukunaga and Hostetler (1975), and later generalized by Cheng (1995). It was first used for color image segmentation by Comaniciu and Meer (1997). In recent years, it has been applied to the processing of remote sensing imagery (Cellier et al., 2005; Bo et al., 2009) and to hematite grain segmentation from polarized light images (Borges da Costa et al., 2007).

The mean-shift clustering (MSC) algorithm is based on the iterative shifting of a kernel to the average of the encompassed data points (Cheng, 1995; Comaniciu & Meer, 1997, 2002). As compared to other clustering procedures and to classification methods based on cluster analysis, such as k-means and support vector machines (SVM), it has the advantage of not requiring previous knowledge of the number of phases or the shape of the clusters.

The principal aim of this work is to demonstrate the applicability of MSC to identify and characterize phases present in a sample using XRMs, even in the cases where other techniques have great difficulties, such as archaeological samples and nonstoichiometric minerals, e.g., clay minerals. After a brief presentation of the MSC technique, two sets of XRMs are analyzed and the results compared with the outcomes of PCA and segmentation by multiple thresholding. The first set, from a polished geological sample, was provided by John C. Russ without the phase spectra. However, since these maps were acquired with good statistics and it is easy to identify six major phases by applying the PCA method (Russ, 2006), it appears this is a good example to contrast MSC results with a typical factor analysis technique. The second set is from an archaeological sample of the Aguada Culture, Catamarca Valley, Catamarca, Argentina IV-XI A.C. (Galván Josa et al., 2009). Archaeological samples offer one of the biggest technical challenges for phase identification and classification, since their surfaces are usually rough and have inhomogeneous composition. Particularly, when the paints on archaeological sherds are applied before cooking, new mineral phases appear, which complicate the correct classification.

Materials and Methods

Theory

As in Stork and Keenan (2010), throughout this article, scalars are represented by italics, e.g., n and column vectors are denoted by boldface lowercase letters, e.g., $\mathbf{d}$. Transposition of a vector is represented by superscript T, e.g., $\mathbf{d}^T$.

In XRM acquisition, the sample surface is irradiated with electrons and the intensities, $I(E, \Delta E, x, y)$, of the induced X-ray emissions from positions (x, y), in the energy range from $E - \Delta E/2$ to $E + \Delta E/2$, are measured by an EDS spectrometer, mapped into 8-bit gray level values ($d = 0,1,2,\ldots,255$) and assigned to pixels of coordinates

$(r, c) = (row, column)$, where $r = 0,1,2,\ldots,R-1$ and $c = 0,1,2,\ldots,C-1$. Each energy channel, centered at E, is selected to encompass the energy range of the X-ray photons emitted by the atoms of a specific element during a characteristic transition from an excited state to a lower energy state. The gray levels $d(r,c)$ of an XRM are therefore representative of the local concentrations of the selected element. Pixel coordinates relate to sample surface positions by $(x, y) = (r\Delta x, c\Delta y)$, where Δx and Δy, are the electron probe step sizes in x and y directions, respectively. These are given by $\Delta x = W/C$ and $\Delta y = L/R$, where W and L are the width and the length of the probed region, C and R are the number of probed surface points along the corresponding directions.

If n XRMs are acquired, one for each of a series of elements, identified by one of its characteristic X-ray energies, E, and indexed by $s = 1,2,\ldots,n$, then the gray level values $d_s(rc)$, are directly related to the local chemical composition at the corresponding sample surface positions. The n gray level values, with the same (r,c) coordinates, are the pixel attributes of the resulting multispectral image.

Each multispectral pixel (r, c) may be indexed by an integer $i = Cr + c + 1$, so that $i = 1,2,\ldots,m$, where $m = R \times C$ is the total number of pixels. Its attributes may be represented by a vector $\mathbf{d}_i$ of components d_{si}, i.e., $\mathbf{d}_i = [d_{1i}, d_{2i},\ldots,d_{ni},]^T$. This is a feature vector associated with the chemical composition of the corresponding sample surface position. Feature vectors of chemically similar probed points tend to cluster around their average, $\mathbf{p}_j$, forming high density regions in the feature space, whose dimensions are the gray levels d_s. The vector $\mathbf{p}_j$ is identified as the prototype of the class, or phase j. If during XRM acquisition the X-ray intensities are calibrated to concentrations, then the components of a prototype vector directly correspond to the chemical composition of a phase.

In this context, the problem of phase classification is the problem of determining to which cluster every pixel belongs. Two different situations may occur. In the first, both the number and the chemical composition of the phases are known, i.e., the set of prototype vectors $\{\mathbf{p}_j\}$, where $j = 1,2,\ldots,l$, is given. Then, the problem reduces to classifying each pixel as belonging to the phase whose prototype is closest to its feature vector.

Multiple thresholding is frequently used as a supervised classification method (Russ, 2006). The threshold value of the intensity of each spectral component is the coordinate of a hyperplane perpendicular to the respective axis in the multidimensional feature space, and each pixel is assigned to a phase if it is inside a hyperparallelepiped (shoe box) limited by these planes. So, an assumption is implicitly made about the shape of the pixel clusters in the feature space (they must be separable by hyperplanes perpendicular to the feature axes) making these techniques inappropriate when nonstoichiometric minerals or solid solutions are present. The reason is that variations on the concentrations of any element will stretch the clusters along the direction of the corresponding spectral component in the feature space, and produce overlapping of the projections of different clusters on that axis, thus precluding the partition of the feature space into hyperparallelepipeds, each containing pixels of a single phase. In fact, each hyperparallelepiped may enclose pixels of the tails of other clusters in its neighborhood.

Classification methods like SVM give an answer to this problem (Lizarazo, 2008). In the second, neither the number nor the chemical composition of the phases are known, i.e., the phases are to be discovered. Then, since phases are associated to clusters in the feature space, the problem is to find the centers of these high density regions. Feature space analysis methods like k-means can be used for this search. However, the result may strongly depend on the initial prototypes of the clusters, which are provided either directly or indirectly by the user. Better results are obtained when this initial guess is guided by some previous knowledge of the structure of the feature space, which can be gained with the aid of visualization tools. As the k-means algorithm is usually fast, it is common to run it multiple times with different starting conditions and then compare the results.

MSC

MSC (Fukunaga & Hostetler, 1975) is a procedure for finding data clusters in multivariate datasets based on the iterative shifting of a kernel to the average, or mean, of the encompassed data points in the feature space. After a finite number of mean shifts, and within a precision determined by the user, the kernel will stop shifting when it is centered at a maximum of the density of data points. This is the center of a cluster, whose members have similar coordinates, or feature values. The procedure is repeated with the kernel starting at every data point, which is assigned to the cluster where the kernel stops.

Starting at a point $\mathbf{d}_0$, taken as the initial prototype $\mathbf{p}_j$, of class j, i.e., $\mathbf{p}_j \leftarrow \mathbf{d}_0$, let a kernel function $K(\mathbf{d}_i - \mathbf{p}_j)$ be given, that weights the nearby points $\mathbf{d}_i$ for estimation of their mean. The weighted mean, $\mathbf{m}(\mathbf{p}_j)$, of the points encompassed by K, is

$$\mathbf{m}(\mathbf{p}_j) = \frac{\sum_{\mathbf{d}_i \in N_h(\mathbf{p}_j)} K(\mathbf{d}_i - \mathbf{p}_j)\cdot \mathbf{d}_i}{\sum_{\mathbf{d}_i \in N_h(\mathbf{p}_j)} K(\mathbf{d}_i - \mathbf{p}_j)}, \tag{1}$$

where $N_h(\mathbf{p}_j) = \{\mathbf{d}_i \mid \|\mathbf{d}_i - \mathbf{p}_j\| \le h\}$ is the set of points in the hyperspherical neighborhood of $\mathbf{p}_j$ for which $K \neq 0$.

Gaussian kernel (Cheng, 1995) on the distance to the current prototype has been widely used, particularly in cases for which some directions in the feature space are more relevant than others. The simplest kernel, which has been used in the present work to test the validity of this approach, is a homogeneous hypersphere, i.e., a fixed multidimensional distance h, measured from $\mathbf{p}_j$, within which all data points have the same weight:

$$K(\mathbf{d}_i - \mathbf{p}_j) = \begin{cases} 1 & \text{if } \|\mathbf{d}_i - \mathbf{p}_j\| \le h, \\ 0 & \text{if } \|\mathbf{d}_i - \mathbf{p}_j\| > h, \end{cases} \tag{2}$$

where

$$\|\mathbf{d}_i - \mathbf{p}_j\| = \sqrt{(\mathbf{d}_i - \mathbf{p}_j)^T \cdot (\mathbf{d}_i - \mathbf{p}_j)} = \sqrt{\sum_{s=1}^{n} (d_{si} - p_{sj})^2}, \quad (3)$$

is the euclidean distance between points $\mathbf{d}_i$ and $\mathbf{p}_j$, and h is the radius of the hypersphere, or bandwidth.

For the kernel given by equation (2), the summation $\sum_{\mathbf{d}_i \in N_h(\mathbf{p}_j)} K(\mathbf{d}_i - \mathbf{p}_j)$ in the denominator of equation (1) is just the number $|N_h(\mathbf{p}_j)|$ of points in $N_h(\mathbf{p}_j)$.

After calculating the mean, the MSC algorithm sets $\mathbf{p}_j \leftarrow \mathbf{m}(\mathbf{p}_j)$, i.e., the center of the kernel is shifted from $\mathbf{p}_j$ to $\mathbf{m}(\mathbf{p}_j)$, which then becomes the new $\mathbf{p}_j$. These two steps are repeated until $\mathbf{m}(\mathbf{p}_j)$ converges to a fixed $\mathbf{p}_j$, i.e., $\mathbf{m}(\mathbf{p}_j) = \mathbf{p}_j$. This final $\mathbf{p}_j$ is the prototype of class j, to which the initial point $\mathbf{d}_0$ is said to belong. Thus the output of this run is both the detection of a cluster in the feature space, and the assignment of the initial point to the corresponding class. After repeating this run for every data point (every pixel in the multispectral image), both the distribution of clusters in the feature space and the phase distribution of the imaged sample are revealed.

The vector that points from the old to the new $\mathbf{p}_j$ is called the mean-shift vector. If the data points are viewed as samples of a multivariate probability density function of finding a feature vector in a differential neighborhood of $\mathbf{d}_i$, then the mean-shift vector is an estimate of its local gradient. The track of the consecutive mean-shift vectors is a path from the starting point to a local density maximum. In the image segmentation problem, this function is the probability of finding a pixel with a given set of spectral intensities, so that the final prototype relates to the most probable chemical composition of a phase.

As already mentioned above, no assumption needs to be made about the number or shape of the clusters when applying MSC. It is also simple and straightforward to implement, and is robust under sampling uncertainties. However, care must be taken when choosing the only input parameter, the so-called bandwidth, typically represented by the radius h of the hypersphere. This is not a trivial task, since an inappropriate choice can either cause merging of clusters, or detect local fluctuations in sampled data as clusters. When applied to phase classification, the former implies that different phases are interpreted as a single one, and, the latter, that materials defects or image acquisition artifacts can be detected as additional phases. The use of variable adaptive bandwidths has been proposed (Comaniciu et al., 2001; Comaniciu, 2003) as a general solution to over-segmentation of multiscale patterns, such as textured objects. However, when applied to materials characterization, this method may eliminate minor phases. Misclassification is better resolved in materials phase analysis by postprocessing, when spatial information may be added via morphological operations (Russ, 2006).

The alternative proposed in this work for the choice of this parameter is intended to give an initial guess for the bandwidth, which may help the user to achieve the appropriate value for this parameter, according to the particular sample under analysis. Bearing in mind that the scattering of data in the feature space are mainly due to the experimental uncertainties associated to the corresponding measured intensities, a first estimate for the bandwidth can be taken as the average of the uncertainties assessed for the set of all the points constituting the feature space. An upper bound for the uncertainty associated to a point $\mathbf{d}$ of the feature space can therefore be written as

$$\sigma_d = \sqrt{\sum_{s=1}^{n} \sigma_{d_s}^2}, \quad (4)$$

where σ_{d_s} is the uncertainty corresponding to the s'th intensity (coordinate) of $\mathbf{d}$. Since the major source of error in X-ray mapping comes from counting statistics, the value taken for σ_{d_s} is the square root of the corresponding intensity. The criterion suggested in the present approach is that the initial guess for h should be at least $\sigma_{\mathbf{d}}$.

Sample Images

Two sets of XRMs were analyzed in order to evaluate the MSC algorithm as a tool to perform materials phase classification. For each set of XRMs, MSC and PCA were applied to obtain the number and distribution of phases and the results were compared. The first set, provided by Russ (2006), is composed of the individual 256 × 199 gray scale (8-bits) images from each of the characteristic X-ray signals of nine elements present in a polished section of a geological sample (Al, Ca, Fe, K, Mg, Na, O, Si, and Ti).

The second set of XRMs, acquired with an EDS equipped LEO 1450 VP SEM (LEO Electron Microscopy Ltd., Cambridge, UK), corresponds to 8-bit 128 × 100 maps from an archaeological sample, namely a piece of Portezuelo style pot sherd (radiocarbon age 600–900 AC) from the Catamarca Valley (Galván Josa et al., 2009). The Portezuelo style is characterized by a very fine ware, with very complex and highly variable manufacturing and decorative techniques (Bertolino & Fabra, 2003; Bertolino et al., 2009). One of the most outstanding characteristics is its noticeable polychromy. In the selected sample, decorative motives are painted in burgundy, reddish, black and white, as can be seen in Figure 1. The X-ray spectra taken at specific zones of each color, show that the white paint has a high Ca content, the black one is associated with the presence of Fe and Mn (plus minor contents of Ca), the burgundy has Fe, Mn, and Ca, and the reddish is related to Fe and Ca.

Implementation

Both MSC and PCA algorithms used in this work were implemented in Matlab® environment. The MSC implementation is an extended version of Bart Finkston's code (Finkston, 2006) that has been modified to accept multi or hyperspectral images as input data. In our extended code, the elements of the $m \times n$ input matrix are the gray scale values of the m pixels in each of the n individual 8-bit images. The function *princomp* used for the PCA implementation is part of the Matlab® standard library. It performs a

Figure 1. Optical photography of the Aguada Portezuelo sherd sample. The area mapped in the scanning electron microscopy-energy-dispersive spectrometry has been highlighted.

PCA on the $m \times n$ data matrix, where rows correspond to observations (pixels) and columns to variables (gray levels corresponding to the intensities of the characteristic X-rays of each element). The output is the set of principal components in decreasing order of significance. They are defined by the coefficients of the uncorrelated linear combinations of the original data whose variances are as large as possible. Segmentation by multiple thresholding can be accomplished by a variety of image processing software packages. In this work, the software QuantiPhase, developed in a previous work advised by one of the authors (Miranda et al., 2004), was chosen due to its ability to set multiple threshold levels simultaneously. The thresholded binary images depict regions of elementary concentrations which are characteristic of certain phases. These are then blended by AND operations in order to take into account the contributions of the different spectral components. Additionally, morphological filtering is needed during this process in order to remove noise.

After running MSC, class labels j, assigned to every pixel, are mapped into unique colors, according to a user-defined lookup table (LUT). In spite of the arbitrariness of the particular choice of colors, the number and the distribution of phases in the output image is invariant under LUT changes. The resulting phase classification takes into account all the information contained in the input images.

On the other hand, after running PCA only a visual representation of the phase distribution is produced by assigning the most significant components to the color channels of an output image. Each color component of every pixel in the output image is then determined by a particular linear combination of the gray levels of the corresponding pixels in the input images. These combinations must be rescaled in order to remain within the range of intensity levels of every channel (usually 256). Hence, colors are not class labels, and, therefore, another procedure is needed in order to classify pixels of similar colors as belonging to the same phases.

Computationally, the PCA algorithm runs much faster than the MSC algorithm, whose execution time greatly depends on the number and size of the input image files and on the choice of the bandwidth. However, the number and the distribution of phases in the output image depend on the choice of both the content of the color channels and the color segmentation algorithm. The output of multiple thresholding is a color-labeled phase distribution image. However, appropriate segmentation is achieved only after many sequences of thresholding, morphological filtering, and boolean operations supervised by the user. The various threshold levels and filtering parameters are arbitrarily chosen by the user; this is a tedious and time-consuming task whose results are subject to many uncertainties.

With the aim of knowing the functional dependency of the classifications phases as a function of bandwidth, several runs of MSC code were performed in a wide range of bandwidth values.

Results and Discussion

The first set of XRMs (Russ, 2006) is shown in Figure 2. The results of PCA were presented and discussed in the original publication. A visual representation of the phase distribution in the sample, shown in Figure 3a, was produced from those results by using the three most significant components, as described in the previous section. Even though this image contains 83% of the information contained in the original image set, it is not a truly phase-segmented image, as pointed out in the previous section. In fact, this image is not even segmented, because pixel values are just linear combinations of the gray levels in the input images. Since XRMs are naturally noisy, so is the output image, whose colors vary from pixel to pixel. The local fluctuations of the pixel colors are better visualized in Figure 3b, where the region outlined in Figure 3a is zoomed in.

While phase classification on a pixel-by-pixel basis requires further processing, the number of phases can be inferred from colocalization plots, i.e., from the two-dimensional (2D) projections of the 9D pixel feature space whose dimensions are the principal components. Clusters in this feature space are identified with phases and counted in the colocalization plots.

The results of multiple thresholding are shown in Figure 3c, where the unclassified pixels are painted black. Six phases are clearly identified by this procedure, which correspond to the colored regions, adding up 86.94% of the total area. The outlined region is zoomed in Figure 3d.

A typical MSC result is shown in Figure 3e. It is a color-labeled image, where seven phases can be clearly seen. In Figure 3f the outlined region, containing the seventh phase, is zoomed in to stress that a single color is attributed to each phase.

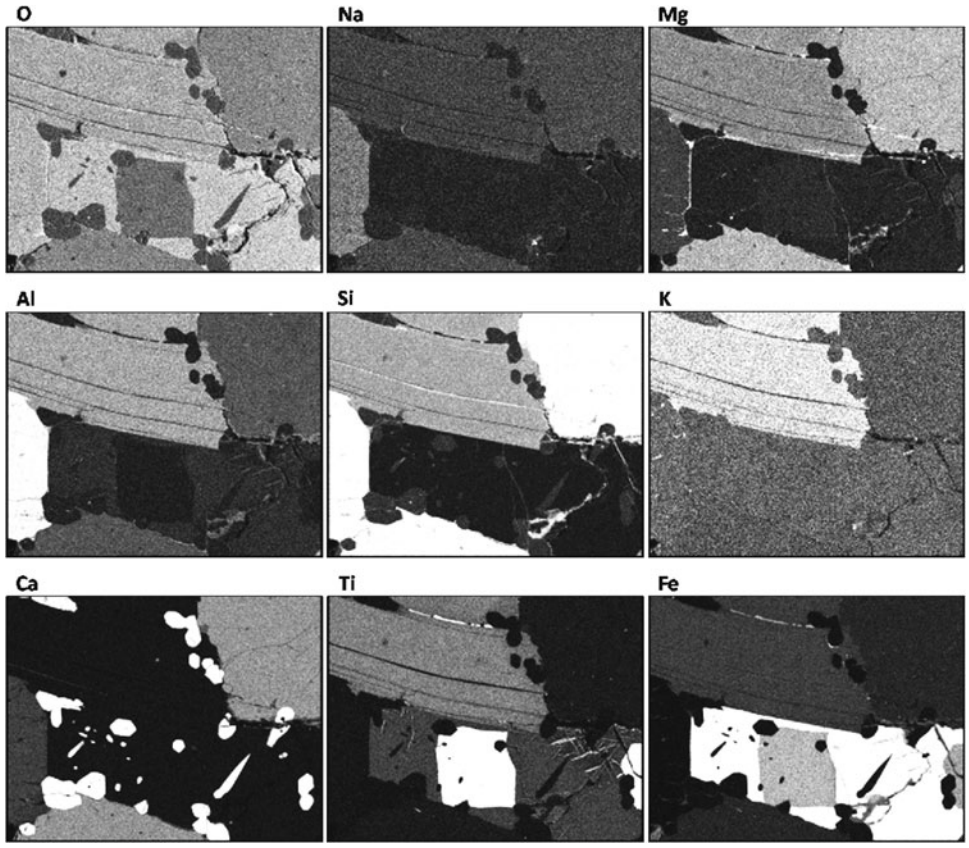

Figure 2. Scanning electron microscopy images of a polished sample of mica provided by Russ (2006). The individual X-ray maps show the distribution of the corresponding elements within various minerals in the sample.

After applying the MSC method, the quantification of phases by area fractions can be readily performed. In all cases, for values of the bandwidth in this range, the area fractions of the minor phases are below 0.5%, as shown in Figure 4, where the results for $h = 85$ are shown. This has been used as an heuristic criterion to consider as real phases only those with area fractions above 0.5%.

The MSC results depend on the particular choice of the bandwidth, h, as can be seen in Figure 5. As pointed out in the Materials and Methods section, small values of this parameter lead to an artificially high number of clusters, while this number goes to one when the bandwidth is comparable to the dynamic range. The question is then how to find the correct result, and the answer must be given on the basis of the user knowledge and expertise about the phase structure of the samples under concern and on the experimental techniques.

The plateau in Figure 5 suggests that the bandwidth that produces appropriate results lies in the range between 55 and 120, for which the mean-shift analysis detects a number of phases between six and eight. Although the average value of this plateau suggests seven phases, in order to be conclusive at this point further information must be provided. Nevertheless, it is important to stress that the MSC algorithm shows some additional structure, with an area fraction of about 2%, which could be studied in better detail.

With the aim of comparing the results obtained by MSC and PCA for the geological sample, a 3D colocalization graph was built with the three most significant components obtained by PCA, as shown in Figure 6. Each point in this graph was colored with the same LUT used in Figures 3c and 4. Six clusters are clearly distinguished in the colocalization plots of component #1 versus component #2 and component #2 versus component #3 (shown in Russ, 2006), which are 2D projections of the clusters seen in Figure 6. The seventh region (brown colored) can be suggested only after the use of MSC, since this method labels the pixels which are mixed up in the 3D colocalization plot. Whether this region is a true phase or, e.g., a poor spectral signature due to the noticeable cracks in the specimen, is a question to be answered by the analyst. What is important to stress here is that MSC allows a more detailed inspection of the sample than PCA.

Table 1 displays the area fractions of phases identified through segmentation by multiple thresholding and MSC. It can be readily seen that the shoe box method has not detected the turquoise colored phase and that many pixels remain unclassified (13.06%), while MSC closure is almost 100%.

In order to test the approach developed here, a set of XRMs was acquired for the archaeological sample described in the Sample Images section. These correspond to the K X-ray lines of Al, Si, Fe, Ca, and Mn (see Fig. 7); they are

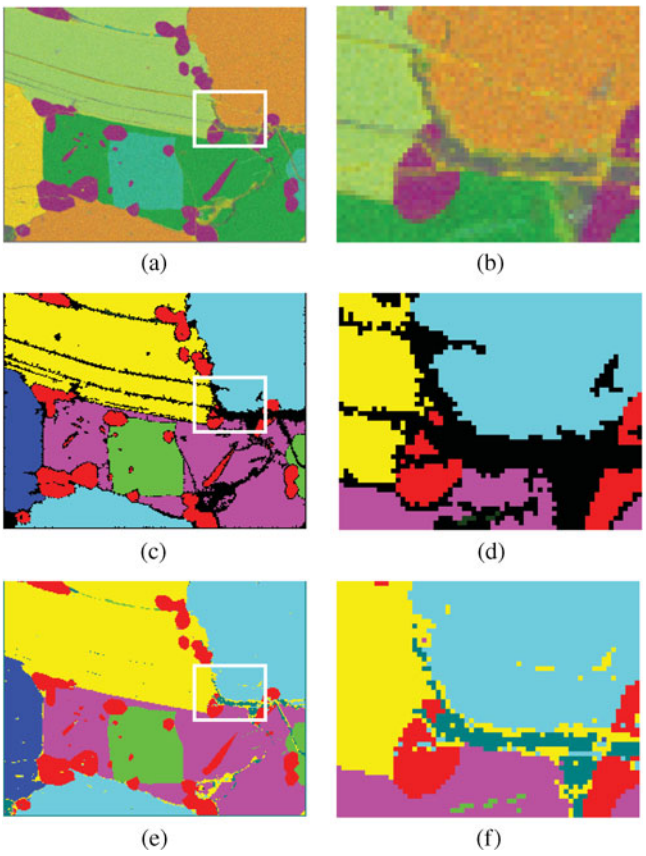

Figure 3. Color representation of the phase distribution in the geological sample of Figure 2 produced by (**a**) assigning the three most significant components obtained by principal components analysis to the color channels of the image, (**c**) ANDing morphologically filtered thresholded images of different spectral components and (**e**) using a lookup table to represent class labels obtained by mean-shift clustering ($h = 85$). Zoomed details of images (**a**), (**c**), and (**e**) are shown in images (**b**), (**d**), and (**f**), respectively.

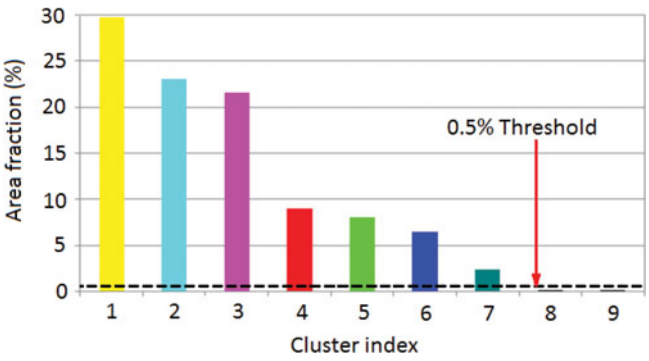

Figure 4. Area fractions of the phases detected in the geological sample of Figure 2 by mean-shift clustering with $h = 85$. All phases with area fractions below 0.5% have been neglected.

more difficult to analyze, since they present poor statistics due to the intrinsic characteristics of the sample (inhomogeneous composition, presence of pores, variable thickness of the surface paints, sample not perfectly flat, etc.). Particularly, it is important to bear in mind that, for XRMs, each pixel value is determined by the chemical composition of

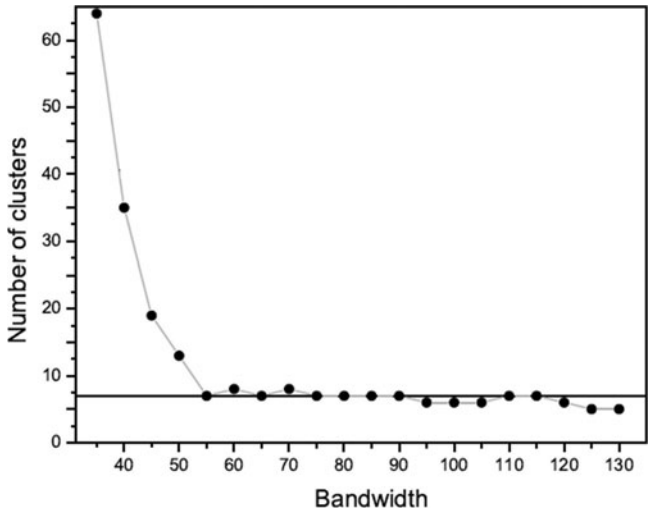

Figure 5. Number of real phases (clusters) detected as a function of the bandwidth. The full line is drawn to outline the plateau corresponding to seven phases.

the material encompassed by the interaction volume, which may also include phase boundaries and defects. Besides, the process of induced X-ray emission is stochastic. Therefore, XRMs are naturally noisy, and the precision to which the intensity values or gray levels can be determined is limited. As a result, isolated pixels are generated, which may be interpreted as new clusters, and a particularly high number of clusters may result. In order to circumvent this problem the original maps were first submitted to a 5×5 Gaussian filtering (Russ, 2006) (i.e., pixel values were substituted by a neighborhood weighted average) and then analyzed by PCA and MSC.

The results obtained after the application of PCA to the XRMs of the Portezuelo sample are shown in Table 2. In this case, 93% of the information is contained in the first three components. The respective colocalization maps do not allow detection of more than two phases. However, the phase distribution obtained by combining these components, shown in Figure 8a, where they were assigned to the R, G, and B channels, respectively, suggests that three or four phases may exist (after contrast expansion). On the other hand, when the MSC analysis is applied to this sample

Table 1. Area Fractions of Phases Identified through Segmentation by Multiple Thresholding and MSC.

Phase	Shoe Box (%)	MSC[a] (%)
Yellow	24.85	29.74
Cyan	22.12	23.03
Magenta	18.33	21.49
Red	7.63	9.00
Green	7.79	7.95
Blue	6.22	6.43
Turquoise	—	2.33
Total	86.94	99.97

[a]MSC, mean-shift clustering.

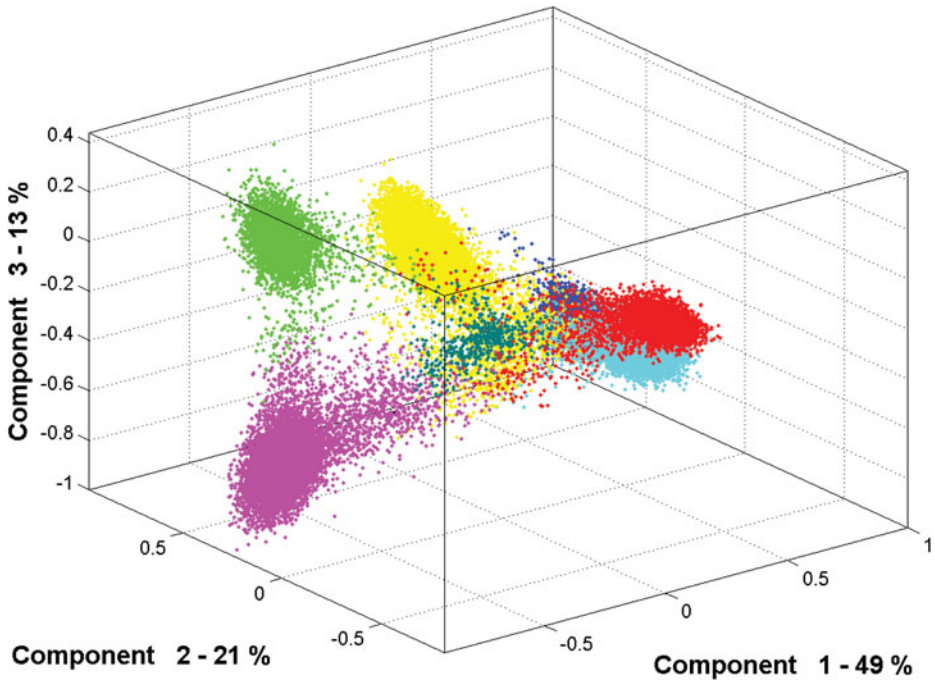

Figure 6. Identification of the phases detected by mean-shift clustering (MSC) in the three-dimensional colocalization plot of the three most significant components obtained by principal components analysis. The colors were assigned according to the MSC lookup table used in Figure 3c.

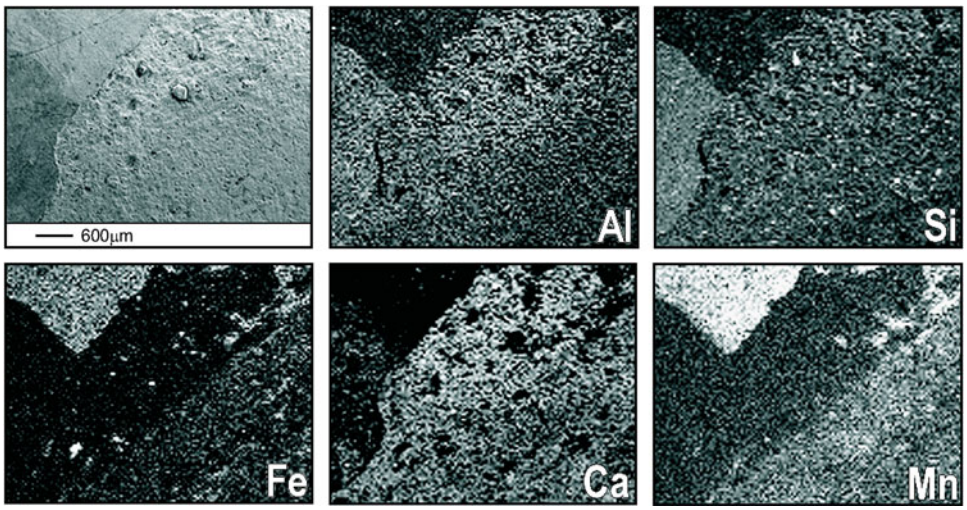

Figure 7. Secondary electron image and X-ray maps of Aguada Portezuelo sherd sample, showing the distribution of the different elements recorded.

Table 2. Coefficients Obtained by Principal Components Analysis (PCA) for the Aguada Portezuelo Sherd Sample.

PC	Significance (%)	Al	Ca	Fe	Si	Ti
1	51.4	−0.5597	−0.6068	0.2269	0.1577	−0.4921
2	28.9	0.2293	−0.7280	0.0072	0.0175	0.6458
3	12.2	−0.7917	0.1902	−0.2426	−0.1606	0.5025
4	6.0	0.0866	−0.2555	−0.7782	−0.4831	−0.2970
5	1.5	0.0012	−0.0184	0.5329	−0.8460	−0.0042

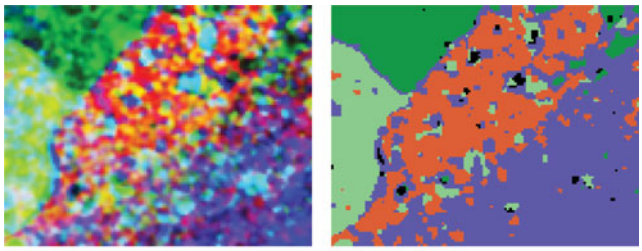

Figure 8. Phase distribution of the Aguada Portezuelo sherd sample as revealed by: (**a**) RGB contrast-expanded image of the three most significant components obtained by principal components analysis and (**b**) color labeling of the pixels belonging to the same clusters detected by mean-shift clustering of the five X-ray maps of Figure 7 (after 5×5 Gaussian filtering).

following the same procedure described above for the analysis of the geological sample, four phases are clearly detected as shown in Figure 8b, in accordance with the optical observation of the sample. This result was obtained for a bandwidth $h = 10$, which detects 45 clusters, of which 41 have been disregarded, since their area fractions are $<0.5\%$ and amount to only 1.1%.

The isolated regions assigned to the cluster corresponding to the white paint in Figure 8b suggest that, the black and red colors were applied to the surface after it was painted white.

Conclusions

In this work, a MSC algorithm was implemented to perform materials phase classification from multispectral images and successfully applied to XRMs of two different samples. This approach was compared with a frequently used multivariate statistical technique, namely the PCA described in Russ (2006). The assignment of a class (phase) label to each pixel is an important advantage of MSC, since there is no need for an additional segmentation algorithm. On the other hand, MSC does not require any previous knowledge neither of the number nor of the composition of the phases sought. This makes MSC a particularly useful tool for exploratory research, assisting phase identification of unknown samples.

When applied to the images of the geological sample analyzed, MSC indicates the same number of major phases as PCA and shoe box; however, it suggests that a seventh minor phase may exist. In addition, when compared to segmentation by multiple thresholding, the empirical reject rate (Shapiro & Stockman, 2001) of MSC is quite low (0.03%) whereas for shoe box is as large as 13.06%. On the other hand, in the case of the archaeological sample, MSC analysis clearly delineates four phases allowing differentiation between the white and burgundy paints, in accordance with the optical observation of the sample.

The results obtained by MSC show that the method proposed is very useful for the characterization of regions of well-defined composition, and robust when the sample preparation conditions are not favorable for the imaging technique, as in the case of the archaeological paints studied here.

Finally, the principles and ideas presented in this paper for the treatment of multispectral images, which we have applied to XRMs, are also applicable to combined datasets, i.e., combinations of images produced by different techniques (Ding & Colpan, 2006; MacRae et al., 2009) or acquired under varying imaging conditions (Pirard et al., 2007; Borges da Costa et al., 2007). Irrespective of the physical origin of the information content of the channels, bands or components of an image, better results are expected to be obtained when complementary information is gained by the addition of a new dimension in the feature space (of course, a compromise with the well known "curse of dimensionality" must be established). The essential requisite to apply MSC to multispectral or multimodal images, is the coregistration of local information to the same pixel coordinates, so that pixels can be mapped into a multidimensional feature space in which they cluster around common properties.

Acknowledgments

This work was partially supported by AUGM and CAPES. The authors wish thank to Dr. John Russ for providing images, and Marcos A.Z. Vasconcellos for the valuable discussions and suggestions.

References

Allen, J.L., Johnson, C.L., Heumann, M.J., Gooley, J. & Gallin, W. (2012). New technology and methodology for assessing sandstone composition: A preliminary case study using a quantitative electron microscope scanner (QEMScan). In *Mineralogical and Geochemical Approaches to Provenance: Geological Society of America Special Paper*, Rasbury, E.T., Hemming, S.R. & Riggs, N.R. (Eds.), vol. 487, 177–194. Boulder, CO: The Geological Society of America.

Bentz, D.P., Stutzman, P.E., Haecker, C.J. & Remond, S. (1999). SEM/X-ray imaging of cement-based materials. In *Proceedings of the 7th Euroseminar on Microscopy Applied to Building Materials*, Pietersen, H.S., Larbi, J.A. & Janssen, H.H.A. (Eds.), pp. 457–466. Delft, the Netherlands: Delft University of Technology.

Bertolino, S.R. & Fabra, M. (2003). Provenance and ceramic technology of pot sherds from ancient Andean cultures at the Ambato valley, Argentina. *Appl Clay Sci* **24**, 21–34.

Bertolino, S.R., Galván, V., Carreras, A., Laguens, A., De La Fuente, G. & Riveros, A. (2009). X-ray techniques applied to surface painting. *X-Ray Spectrom* **38**, 95–102.

Bo, S., Ding, L., Li, H., Di, F. & Zhu, C. (2009). Mean shift-based clustering analysis of multispectral remote sensing imagery. *Int J Rem Sen* **30**(4), 817–827.

Borges da Costa, J.A.T., Rosa, M., Takehara, L., Ornellas, M.C. & Vasconcellos, M.A.Z. (2007). Grain segmentation of hematite-rich ore by multivariate analysis of polarized light image stacks. In *VIII Simpósio Brasileiro de Minério de Ferro*. Salvadore, Bahia, Brazil, September 18–27, 2007. São Paulo, SP: Associação Brasileira de Metalurgia e Materiais.

Carling, G.T., Fernandez, D.P. & Johnson, W.P. (2012). Dust-mediated loading of trace and major elements to Wasatch Mountain snowpack. *Sci Total Environ* **432**, 67–77.

Cellier, F., Oriot, H. & Nicolas, J.M. (2005). Introduction of the mean shift algorithm in SAR imagery: Application to shadow extraction for building reconstruction. In *Proceedings of the Earsel 3D Remote Sensing Workshop*, Porto, Portugal, June 10–11, 2005.

Cheng, Y. (1995). Mean shift, mode seeking, and clustering. *IEEE Trans Pattern Anal Machine Intell* **17**(8), 790–799.

Comaniciu, D. (2003). An algorithm for data-driven bandwidth selection. *IEEE Trans Patt Anal Mach Intell* **25**(2), 281–288.

Comaniciu, D. & Meer, P. (1997). Robust analysis of feature spaces: Color image segmentation. *IEEE Proceedings Conf Computer Vision Pattern Recognition*, pp. 750–755.

Comaniciu, D. & Meer, P. (2002). Mean shift: A robust approach toward feature space analysis. *IEEE Trans Pattern Anal Machine Intell* **24**, 603–619.

Comaniciu, F., Ramesh, V. & Meer, P. (2001). The variable bandwidth mean shift and data-driven scale selection. In *Proceedings of the Eighth International Conference on Computer Vision*, vol. 1, pp. 438–445. Washington, DC: IEEE.

Ding, Q. & Colpan, M. (2006). Decision tree induction on hyperspectral cement images. *Int J Inform Math Sci* **2**(3), 169–175.

Finkston, B. (2006). Mean-shift clustering. Available at http://www.mathworks.com (accessed October, 19 2010).

Fukunaga, K. & Hostetler, L.D. (1975). The estimation of the gradient of a density function, with applications in pattern recognition. *IEEE Trans Info Theory* **21**(1), 32–40.

Galván Josa, V., Bertolino, S., De La Fuente, G., Riveros, J. & Castellano, G. (2009). Caracterización de Pinturas Arqueológicas Mediante el Procesamiento de Mapas de Rayos X. *Acta Microscopica* **18**(Suppl C), 385–386.

Gernet, U. (2008). Comparing the Si(Li)-detector and the silicon drift detector (SDD) using EDX in SEM. In *14th European Microscopy Congress*, Luysberg, M., Tillmann, K. & Weirich, T. (Eds.), pp. 697–698. Aachen, Germany: Springer Berlin Heidelberg.

Götze, J., Plötze, M., Götte, T., Neuser, R.D. & Richter, D.K. (1997). Cathodoluminescence (CL) and electron paramagnetic resonance (EPR) studies of clay minerals. *Mineral Petr* **76**, 195–212.

Harris, R.J. (2001). *A Primer of Multivariate Statistics*, 3rd ed., pp. 40–41. Mahwah, NJ: Lawrence Erlbaum Publishers.

Humphreys, F.J. (2001). Grain and subgrain characterisation by electron backscatter diffraction. *J Mater Sci* **36**, 3833–3854.

Jain, A.K. (2010). Data clustering: 50 years beyond K-means. *Patt Recog Lett* **31**, 651–666.

Keenan, M.R. (2008). Exploiting spatial-domain simplicity in spectral image analysis. *Surf Interface Anal* **41**, 79–87.

Kotula, P.G. (2002). Spectral imaging: Towards quantitative X-ray microanalysis. *Microsc Microanal* **8**(Suppl 2), 440–441.

Kotula, P.G. & Keenan, M.R. (2006). Application of multivariate statistical analysis to STEM X-ray spectral images: Interfacial analysis in microelectronics. *Microsc Microanal* **12**, 538–544.

Kotula, P.G., Keenan, M.R. & Michael, J.R. (2003). Automated analysis of SEM X-ray spectral images: A powerful new microanalysis tool. *Microsc Microanal* **9**, 1–17.

Lizarazo, I. (2008). SVM-based segmentation and classification of remotely sensed data. *Int J Remote Sens* **29**(24), 7277–7283.

MacRae, C.M., Wilson, N.C. & Brugger, J. (2009). Quantitative cathodoluminescence mapping with application to a Kalgoorlie scheelite. *Microsc Microanal* **15**, 222–230.

MacRae, C.M., Wilson, N.C., Johnson, S.A., Phillips, P.L. & Otsuki, M. (2005). Hyperspectral mapping combining cathodoluminescence and X-ray collection in an electron microprobe. *Microsc Res Tech* **67**(5), 271–277.

Miranda, A.N., Pinheiro, D.P. & Borges da Costa, J.A.T. (2004). QuantiPhase, Informtica, Universidade Federal de Santa Maria, Brazil. Available at http://www-usr.inf.ufsm.br/~miranda/QuantiPhase.php (accessed March 1, 2013).

Neal, B. & Russ, J. (2004). Principal components analysis of multispectral image data. *Microsc Today* **12**, 36–38.

Pirard, E. (2004). Multispectral imaging of ore minerals in optical microscopy. *Mineral Mag* **68**(2), 323–333.

Pirard, E. & Lebichot, S. (2005). Automated identification of iron oxides under the optical microscope. Mineral Georesources and Geo-Imaging Group, GeomaC Department Belgium.

Pirard, E., Lebichot, S. & Krier, W. (2007). Particle texture analysis using polarized light imaging and gray level intercepts. *Int J Miner Process* **84**, 299–309.

Russ, J. (2006). *The Image Processing Handbook*, 5th ed. Boca Raton, FL: CRC Press.

Shapiro, L. & Stockman, G. (2001). *Computer Vision*. Englewood Cliffs, NJ: Prentice Hall.

Stork, C.L. & Keenan, M. (2010). Advantages of clustering in the phase classification of hyperspectral materials image. *Microsc Microanal* **47**, 1–17.